Electronic Supplementary Material (ESI) for Energy & Environmental Science.
This journal is © The Royal Society of Chemistry 2018

Electronic Supplementary Information (ESI)

Gigantic Enhancement in Electricity Generation in Piezoelectric Semiconductors by Creating Pores as a Universal Approach

Yu-Lun Su,[a] Kapil Gupta,[a] Yu-Liang Hsiao,[a] Ruey-Chi Wang[b] and Chuan-Pu Liu*[ac]

[a] *Department of Materials Science and Engineering, National Cheng Kung University, Tainan 701 (Taiwan)*

[b] *Department of Chemical and Materials Engineering, National University of Kaohsiung, Kaohsiung 81148 (Taiwan)*

[c] *Hierarchical Green-Energy Materials (Hi-GEM) Research Center, National Cheng Kung University, Tainan 701 (Taiwan)*

*Corresponding author E-mail: cpliu@mail.ncku.edu.tw

Keywords: Self-powered nanodevices; simulation; nanogenerator; porous nanowires; strain-gated transistor

Table S1: **The material properties[1,2] of the ZnO NWs for simulation of piezopotential and strain distribution using COMSOL Multiphysics 5.1.**

Material Properties	Values
Poisson's Ratio	0.33
Young's modulus (GPa)	210
Relative permittivity	$\varepsilon_{r11} = 8.5446$, $\varepsilon_{r22} = 8.5446$, $\varepsilon_{r33} = 10.204$, $\varepsilon_{rij} = 0$
Piezoelectric coupling coefficient matrix (C/m^2)	$e_{31} = -0.56$, $e_{32} = -0.56$, $e_{33} = 1.32$, $e_{24} = -0.48$, $e_{15} = -0.48$
Elasticity matrix (GPa)	$C_{11} = 209.7$, $C_{12} = 121.1$, $C_{22} = 209.7$, $C_{13} = 105.3$, $C_{23} = 105.3$, $C_{33} = 211.1$, $C_{44} = 42.3$, $C_{55} = 42.3$, $C_{66} = 44.2$

1. Carlotti, G., Socino, G., Petri, A., & Verona, E., *Appl. Phys. Lett.* **51**, 1889 (1987)
2. Landolt-Bomstein, Numerical Data and Function Relationships in Sciences and Technology (Springer, Berlin, Heidelberg, 1979), Group III, Vol 11.

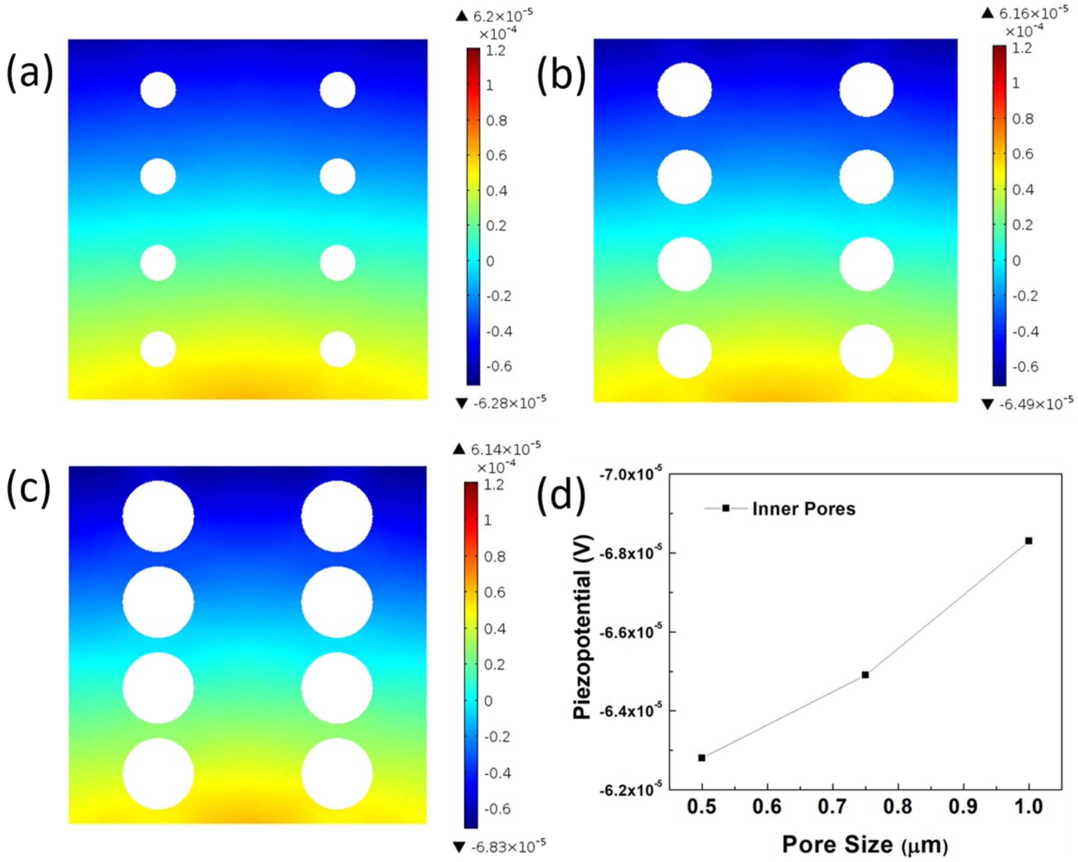

Fig. S1 Piezopotential distribution in porous NW (a cylindrical geometry with height 10 μm and radius 5 μm) under normal compressive force (10 nN) applied to the top surface of NW, with varying pore sizes (radius of spherical pores), (a) 0.5 μm, (b) 0.75 μm, and (c) 1 μm. (d) Comparison of negative piezopotential at the +*c* polar surface as a function of pore size.

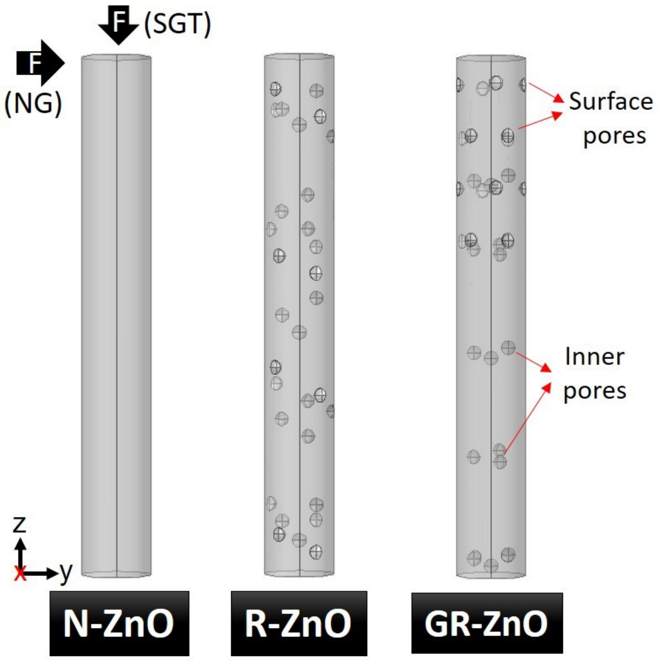

Fig. S2 Three models of ZnO NWs, used for simulation study. Non-porous ZnO NW (N-ZnO), porous ZnO NW with randomly distributed inner and surface pores (R-ZnO), and porous ZnO NW with inner pores following random distribution and surface pores following density gradient distribution (GR-ZnO). Inner and surface pores are indicated in G-ZnO NW.

In this simulation study (Fig. S3), inner and surface pores with gradient distribution are placed at the bottom (Fig. S3b) and top (Fig. S3c) of the NWs, and compared with non-porous NW (Fig. S3a). The negative piezopotential increases from -0.231 V (Fig. S3a) to -0.41 V (Fig. S3b) when the pores are located at the bottom side, and positive piezopotential increases from 0.265 V (Fig. S3a) to 0.454 V (Fig. S3c) when the pores are located at the top. This confirms that the location of pores is very crucial and the impact of spatial distribution of pores is more significant.

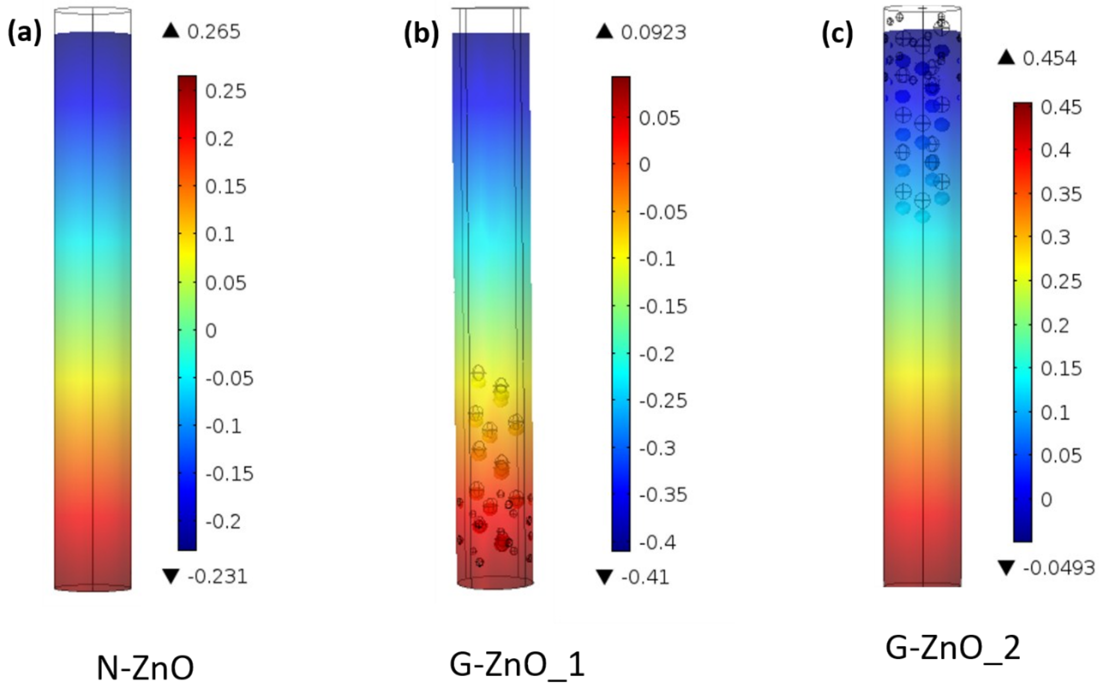

Fig. S3 Piezopotential distribution under normal compressive force (10 nN) applied to the top surface of NW in, (a) non-porous ZnO NW (N-ZnO), and porous ZnO NW with inner and surface pores of density gradient distribution (G-ZnO), (b) at the bottom of NW (G-ZnO_1), and (c) at the top of NW (G-ZnO_2).

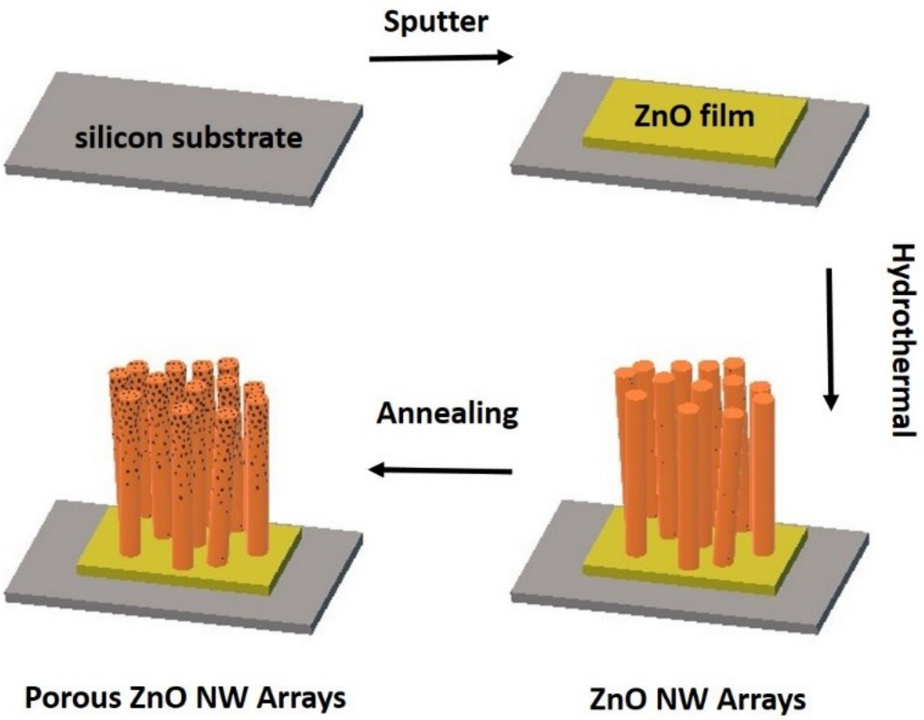

Fig. S4 Schematic of the materials preparation scheme.

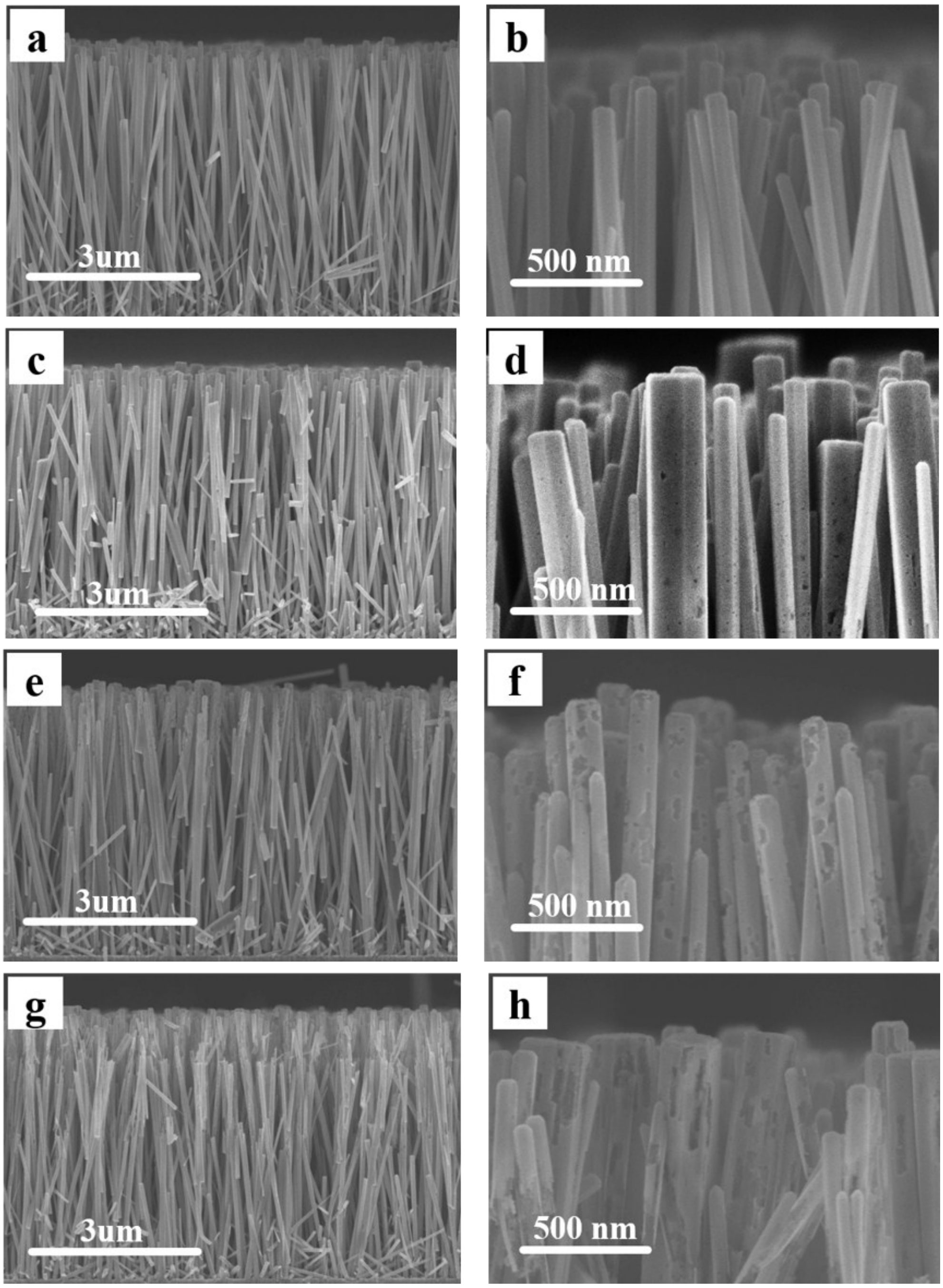

Fig. S5 SEM images of the porous ZnO NWs. (a-b) As-grown ZnO NW arrays, having 100 nm in diameter and 5μm in length with classic hexagonal shaped column. (c-d) 3 h annealed ZnO NW arrays. Diameters of the pores are 5-10 nm and have the feature of gradient pore density. (e-f) 6 h annealed ZnO NW arrays. Diameters of the pores increase to 10-50 nm. The feature of gradient become clearer and have higher pore density. (g-h) 9 h annealed ZnO NW arrays. The porous ZnO NWs are broken due to the over-etching.

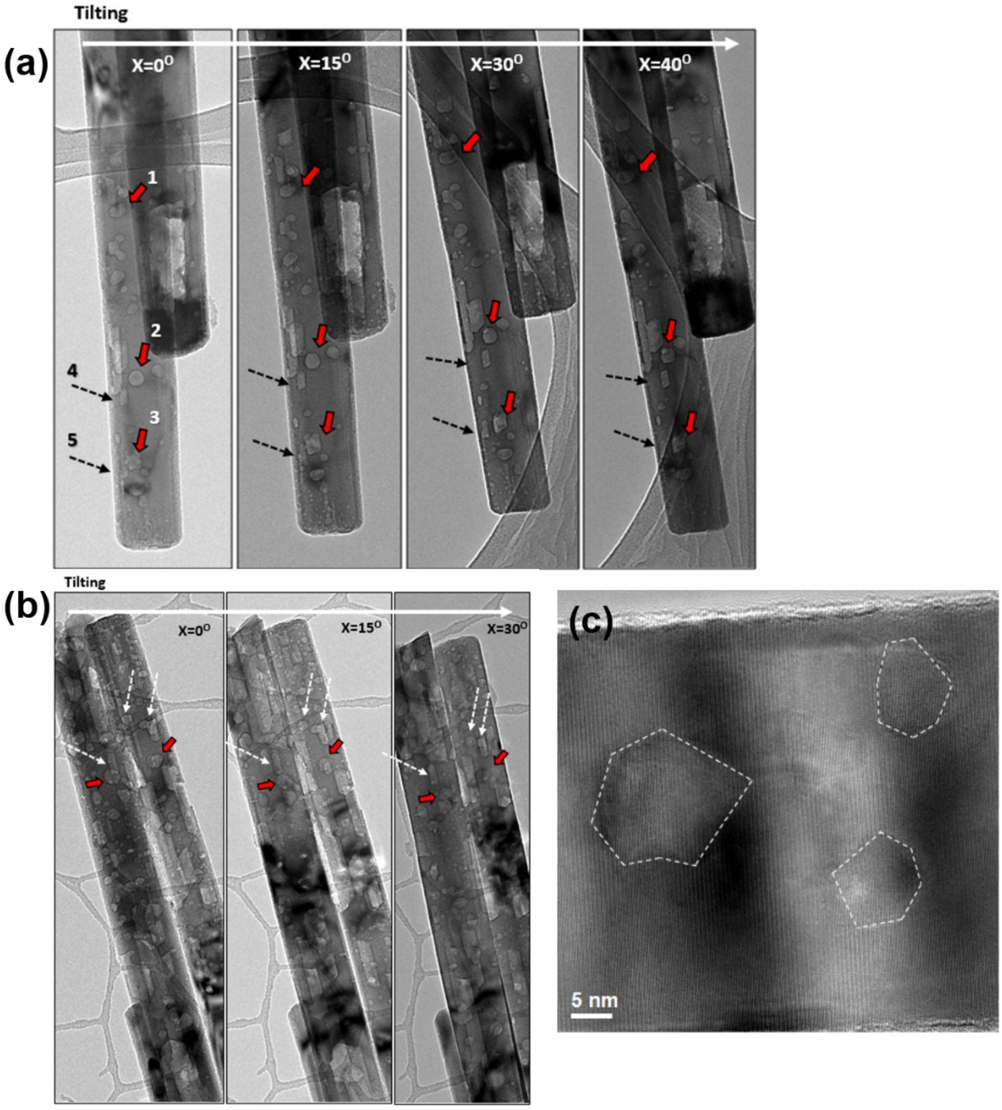

Fig. S6 (a,b) TEM images of porous ZnO NWs hydrogen annealed for 3 h, while rotating the nanowire about its long axis inside TEM. The pores that stay fixed at their positions are inner pores (small red arrow), and pores that move upon rotation are surface pores (white dashed arrow). (c) Random shaped pores in porous ZnO NW showing that the pores are under non-equilibrium conditions.

Porosity calculations

By knowing the types of the pores, porosity can be calculated[20]. For simplicity, the inner and surface pores are considered as one sphere and half sphere. With the help of IMAGEJ, porosity can thus be calculated from TEM images as followed:

$$Porosity = \frac{Volume\ of\ the\ inner\ and\ surface\ pores}{Total\ volume\ of\ porous\ ZnO\ NWs} \times 100\%$$

The results are presented in Table S2.

Table S2. **Porosity with corresponding annealing durations of the three types of the porous ZnO NWs.**

ZnO NWs	0HA-ZnO	3HA-ZnO	6HA-ZnO
Porosity	0	2.6%	5.4%

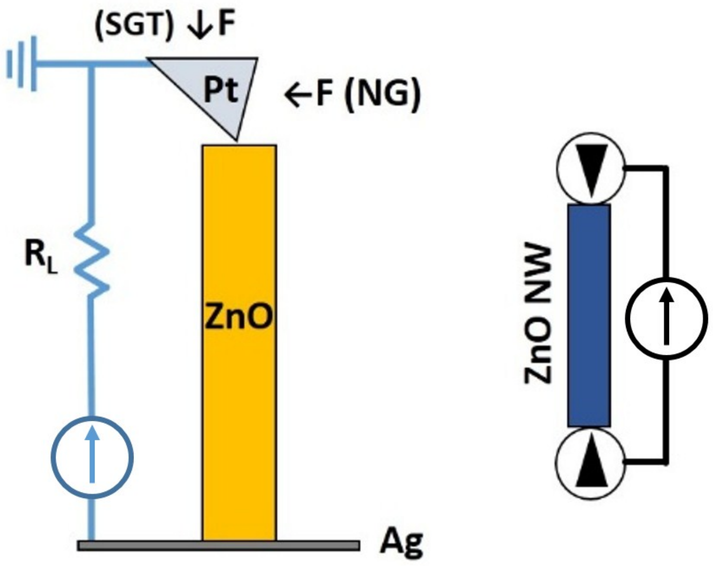

Fig. S7 Schematic diagram of experimental set-up in piezotronic and DC NG measurements, with the equivalent circuit as a back-to-back double Schottky diode shown on the right.

Fitting procedure by using thermionic field emission theory

According to thermionic field emission (TFE) theory,

$$J(V,\phi_b) =- J_{sr}(V,\phi_b)\exp\left[V\left(\frac{q}{kT} - \frac{1}{E_0}\right)\right] \qquad (S1)$$

and the current density under reverse bias is,

$$J_{sr} = \frac{A^*T(\pi qE_{00})^{1/2}}{k}\exp\left(-\frac{\phi_b}{qE_0}\right)\{q(V-\zeta) + \frac{\phi_b}{cosh^2(\frac{qE_{00}}{kT})}\} \qquad (S2)$$

where Φ_b is the effective SBH, q is the electron charge, k is the Boltzmann constant, T is the absolute temperature, A^* is the Richardson constant, ζ is the distance between bottom of the conduction band and Fermi level for *n*-type materials. E_0 and E_{00} are given by,

$$E_0 = E_{00}\coth\left(\frac{qE_{00}}{kT}\right) \qquad (S3)$$

and,

$$E_{00} = \frac{h}{4\pi}[\frac{N_d}{m^*_n\varepsilon_s\varepsilon_0}]^{1/2} \qquad (S4)$$

where N_d is the doping concentration, h is the Planck constant, m^*_n is the effective electron mass, ε_s and ε_0 are relative permittivity for semiconductor materials and vacuum permittivity, respectively.

Moreover, the corresponding change of SBH, related to piezopotential in controlling carrier transport across interfaces of piezotronics, can be derived from the equation below[29].

$$\ln\left[\frac{I(\varepsilon_i)}{I(\varepsilon_0)}\right] =- \Delta\emptyset_{SBH}/kT \qquad (S5)$$

where $I(\varepsilon_i)$ and $I(\varepsilon_0)$ are the current with and without external stresses.

By plotting the curves of logarithmic current density versus voltage, E_0 is first derived from the slope of the curves in the moderate applied voltage range as in Fig. S8. Once

E_0 is known, N_d and the corresponding Φ_b can be obtained from Equations S3-S4, by taking the bulk ZnO values for m^*_n and ε_s.

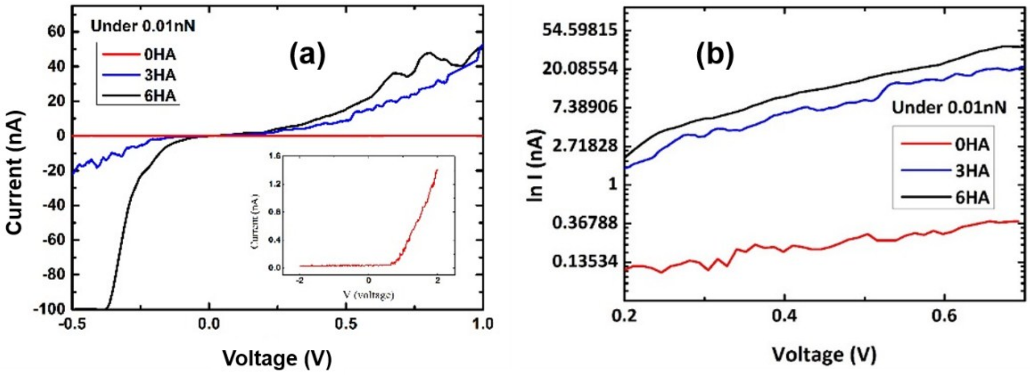

Fig. S8 (a) *I-V* characteristics of the three types of ZnO NWs. Logarithmic plots of the current under positive biases from (a). Linear relationship between In(*I*) and moderate voltages showing the *I-V* characteristics of the three type of ZnO NWs can be described by thermionic field emission theory.

Proposed Mechanisms

Energy band diagrams of a porous ZnO NW along with two contact electrodes are proposed in Fig. S9, incorporating different contributions from hydrogen annealing. First, hydrogen is a type of shallow donor (H_i^+), resulting in increasing carrier concentration and thus the Fermi level (Fig. S9a). Subsequently, oxygen molecules would desorb from the surface of the ZnO NWs causing less depletion region and surface band bending, thereby increasing the conductivity as well as decreasing SBH (Fig. S9b). The first two effects have rendered ZnO NWs more conductive as expressed by higher current density in *I-V* characteristics in Fig. S8. Nevertheless, the greater change of current density change is evidently caused by higher piezopotential induced by pores.

Performance of the single nanowire based piezotronics and nanowire arrays based NGs were greatly enhanced via porous nanostructure. As shown in Fig. S9c, when a compressive stress is applied on the porous ZnO NWs, it experiences a larger change of SBH compare to the non-porous ones. The negative piezopotential present at the Pt-ZnO interface preclude the current flow while the positive piezopotential reveal at Ag-ZnO is screened by free carriers. Situation for the NGs is a little different, mechanical bending upon a lateral force leads to the positive piezopotential in the stretched side surface and negative piezopotential in the compressed side surface as shown in Fig. S9d. Again, pores will cause larger piezopotential difference between two side surfaces. Above all, a decrease in band bending and an increase in carrier concentration as well as porous nanostructure introduced by hydrogen annealing can effectively improve the energy harvesting.

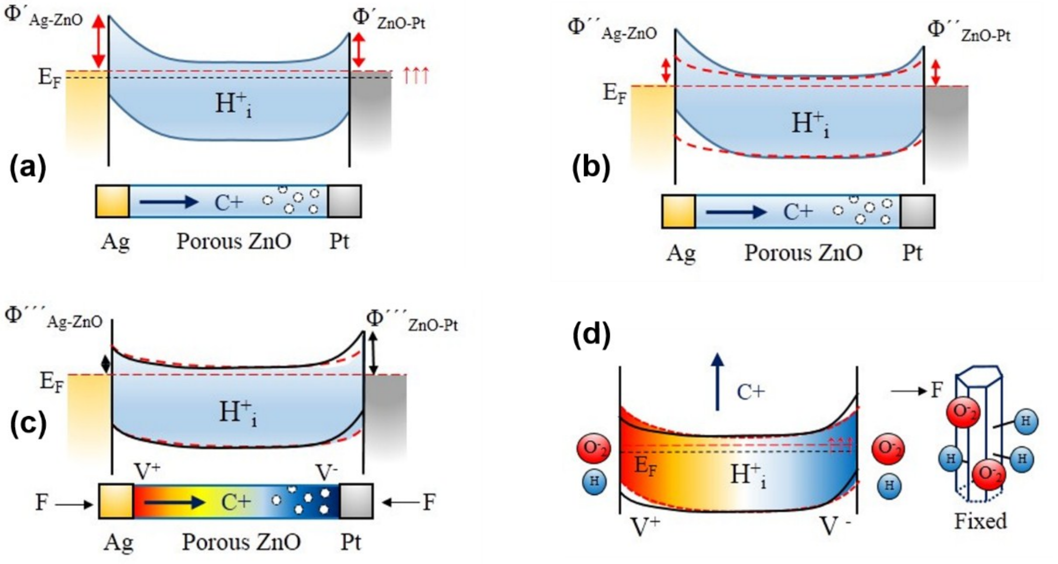

Fig. S9 Schematic of energy band for each key process in our work. (a) As a dopant, hydrogen would increase the carrier concentration and consequently increase the Fermi level (red dash lines). (b) Surface band bending of ZnO is decreased (red dash line) in the absence of oxygen molecules owing to the 500 ^{o}C hydrogen annealing. (c) Under a compressive stress, negative piezopotential increases the SBH at Pt-ZnO interface while positive piezopotential reveals at Ag-ZnO interface may be screened by carriers (black line). (d) Positive piezopotential performs in the stretched side surface and the negative piezopotential in the compressed side surface (black line) upon a shear stress.

Piezoelectric coefficient (d_{33}) measurement

Piezoresponse force microscopy (PFM) images of non-porous (as-grown) and porous (3 h annealed) NWs with the help of PFM in vertical response mode with AC voltage signal are obtained. Fig. S10 shows the PFM images of non-porous (Fig. S10a-c) and porous NW (Fig. S10d-f) at 500, 1000, and 1500 mV AC amplitude. The mean value of piezoresponse of each PFM image is also indicated, which were used to calculate the slope and piezoelectric coefficient (d_{33}) (Fig. S11 and Table S3).

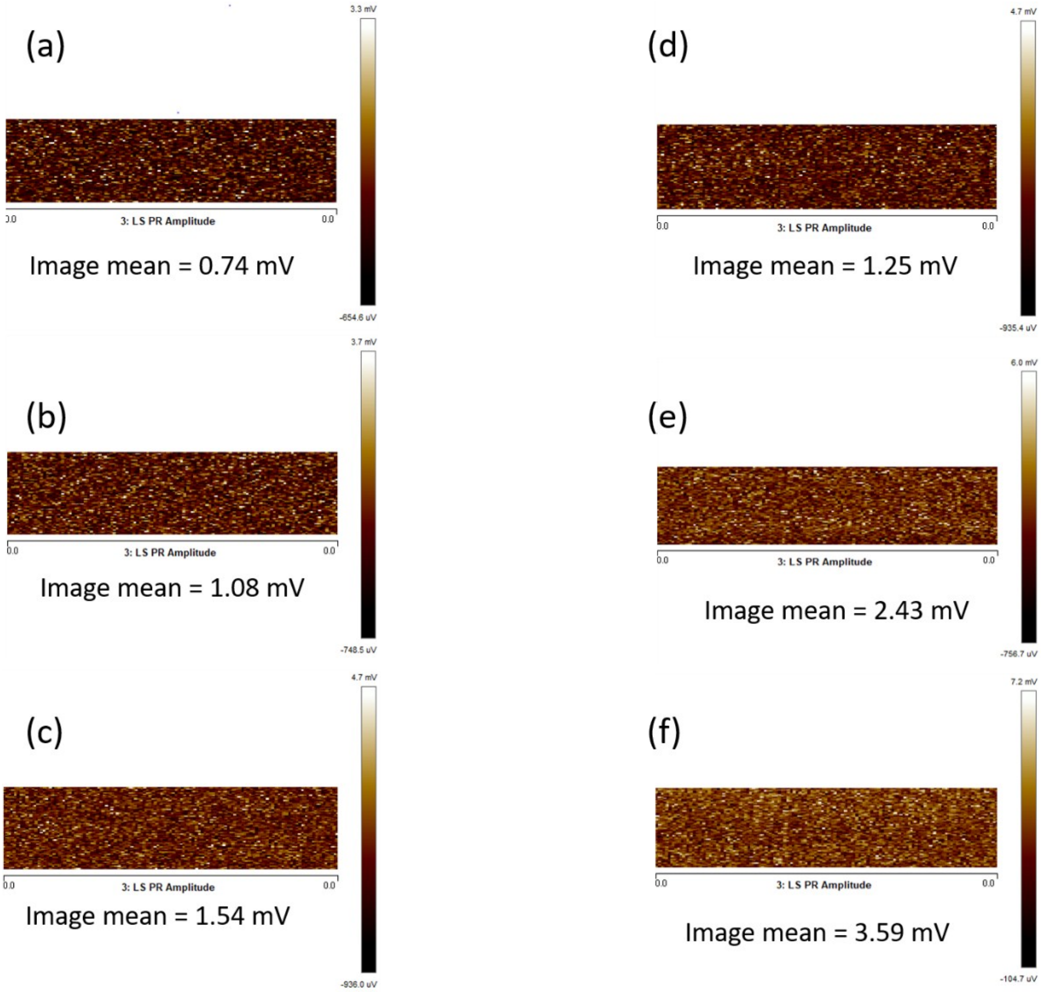

Fig. S10 Piezoresponse force microscopy (PFM) images. PFM images of non-porous (as-prepared) ZnO NW at AC amplitude of (a) 500 mV, (b) 1000 mV, and (c) 1500 mV. PFM images of porous (3 h annealed) ZnO NW at AC amplitude of (d) 500 mV, (e) 1000 mV, and (f) 1500 mV. Mean values of piezoresponse is indicated.

Piezoelectric coefficient (d_{33}) measurements on non-porous (as-grown) and porous (3 h annealed) NWs were performed using converse piezoelectric effect, with the help of PFM in vertical response mode with AC voltage signal, and single point measurements were carried out (Fig. S11). Although, it is easier to investigate the piezoelectric coefficient of 2D thin films using PFM, it is not so straightforward for the case of 1D NWs, due to the lack of a standard sample with similar microstructure to compare the deformation upon voltage application. For this reason, exact piezoelectric coefficient for non-porous (as-grown) and porous (3 h annealed) NWs were not found, however, the slope of piezo-response vs AC amplitude plot is normalized with respect to non-porous NW, as effective d_{33}. Interestingly, it is found that the effective d_{33} for porous NW is 2.89 times that of non-porous NW (Table S3), which proves that the piezoelectric coefficient of porous NWs is higher than the non-porous NWs.

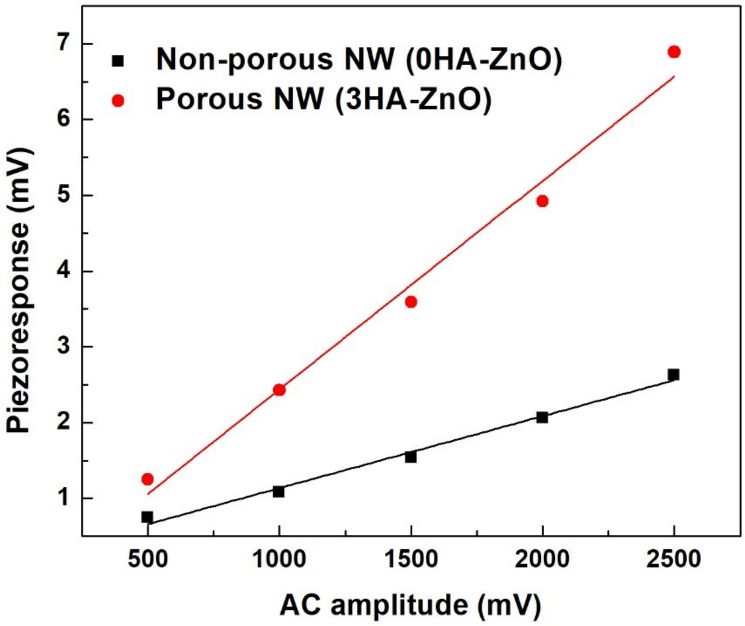

Fig. S11 Piezo-response vs AC amplitude plot for a non-porous ZnO NW (0HA-ZnO) and 3 hour H_2 annealed porous ZnO NW (3HA-ZnO) using PFM. Linear fitting is also shown.

Table S3. The slope of linear fitting in Fig. S11, and effective d_{33} of non-porous and porous ZnO NW**.**

	Non-porous ZnO NW	**Porous ZnO NW**
Slope	9.5×10^{-4}	2.75×10^{-3}
Effective d_{33}	**1**	**2.89**